

Two-way magnetic resonance tuning and enhanced subtraction imaging for non-invasive and quantitative biological imaging

Zhongling Wang^{1,2,11}, Xiangdong Xue^{© 2,11}, Hongwei Lu², Yixuan He², Ziwei Lu³, Zhijie Chen^{© 4,5}, Ye Yuan², Na Tang¹, Courtney A. Dreyer², Lizabeth Quigley⁶, Nicholas Curro⁴, Kit S. Lam^{© 2,7}, Jeffrey H. Walton^{© 2,8}, Tzu-yin Lin⁷, Angelique Y. Louie⁹, Dustin A. Gilbert^{© 6}, Kai Liu^{© 4,5}, Katherine W. Ferrara^{© 10} and Yuanpei Li^{© 2} ⊠

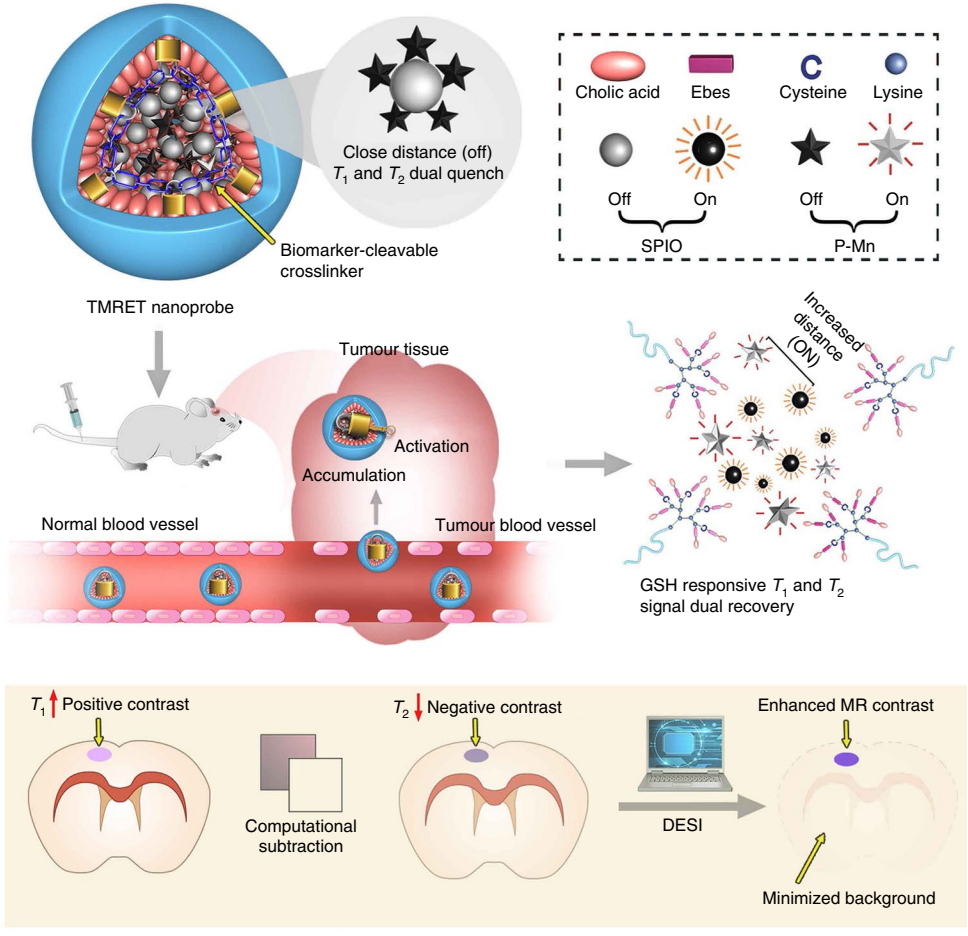
Distance-dependent magnetic resonance tuning (MRET) technology enables the sensing and quantitative imaging of biological targets in vivo, with the advantage of deep tissue penetration and fewer interactions with the surroundings as compared with those of fluorescence-based Förster resonance energy transfer. However, applications of MRET technology in vivo are currently limited by the moderate contrast enhancement and stability of T_1 -based MRET probes. Here we report a new two-way magnetic resonance tuning (TMRET) nanoprobe with dually activatable T_1 and T_2 magnetic resonance signals that is coupled with dual-contrast enhanced subtraction imaging. This integrated platform achieves a substantially improved contrast enhancement with minimal background signal and can be used to quantitatively image molecular targets in tumours and to sensitively detect very small intracranial brain tumours in patient-derived xenograft models. The high tumour-to-normal tissue ratio offered by TMRET in combination with dual-contrast enhanced subtraction imaging provides new opportunities for molecular diagnostics and image-guided biomedical applications.

anometre-scale distance-dependent physical processes have substantially advanced the fundamental understanding of living systems and facilitated the development of new molecular medicines for better patient care¹⁻⁵. Förster resonance energy transfer (FRET) is one such physical process, which is highly sensitive to investigate biological phenomena that produce changes in molecular proximity⁶⁻⁸. However, FRET suffers from low and fluctuating signal intensities from single fluorophores and short observation times due to photobleaching. Nanoplasmonic techniques use distance variations between noble metals to generate a surface plasmon resonance absorption wavelength shift and subsequent colour changes³. Such techniques can overcome the limitations of organic fluorophores and provide a fast and convenient platform to map biological activities^{1,3}. However, together with FRET, the broad applications of these optical techniques may be hampered by their intrinsically low tissue penetration and undesirable photon interactions with the complicated biological environments in the body9. Cheon and co-workers reported the pioneering work on magnetism-based nanoscale distance-dependent magnetic resonance tuning (MRET). MRET opens new possibilities for the non-invasive investigation of biological processes because magnetic resonance imaging (MRI) can provide high-resolution functional and anatomical imaging without being limited by the tissue penetration depth⁹. In MRET, T_1 relaxation is modulated by controlling the distance between a paramagnetic T_1 enhancer and a superparamagnetic quencher. However, the use of T_1 contrast agents in MRET can be compromised by a low sensitivity and an intrinsically low magnetic resonance (MR) relaxivity. The first MRET probes were administrated intratumourally; however, the size, stability and surface properties of these probes need to be further optimized for abroad in vivo application by using systemic injection (in which these probes are exposed to the bloodstream). Furthermore, ¹H MRI typically suffers from a low contrast enhancement with a high background noise from normal tissue, due to the interference from intrinsic ¹H signals in the body¹⁰.

Here we introduce a new two-way magnetic resonance tuning (TMRET) nanotechnology with dually activatable T_1 and T_2 signals. This method is designed to substantially improve the MR contrast and reliability as well as suppress the background signal of MRET. TMRET nanotechnology is constructed by the concurrent encapsulation of a two-way MRET pair, a pheophorbide a–paramagnetic Mn²+ chelate (P–Mn) and a superparamagnetic iron oxide (SPIO) nanoparticle, into a micelle with a structure-dependent stability and stimuli responsiveness (Scheme 1). When the two-way MRET pair is 'locked' closely within the micelle core, the T_1 and T_2 MRI signals are turned 'off'. On interaction with biological stimuli (the 'key'), the T_1 and T_2 MRI signals are dually turned 'on' depending on the increased distance between Mn²+ and SPIO, which is controlled

¹Department of Radiology, Shanghai General Hospital, School of Medicine, Shanghai Jiaotong University, Shanghai, China. ²Department of Biochemistry and Molecular Medicine, UC Davis Comprehensive Cancer Center, University of California Davis, Sacramento, CA, USA. ³Department of Radiology, First Affiliated Hospital of Soochow University, Suzhou, China. ⁴Department of Physics, University of California, Davis, CA, USA. ⁵Department of Physics, Georgetown University, Washington, DC, USA. ⁶Department of Materials Science and Engineering, University of Tennessee, Knoxville, TS, USA. ⁷Division of Hematology/Oncology, Department of Internal Medicine, University of California Davis, Sacramento, CA, USA. ⁸UC Davis NMR Facility, Davis, CA, USA. ⁹Department of Biomedical Engineering, University of California Davis, Davis, CA, USA. ¹⁰Department of Radiology, Stanford University, Palo Alto, CA, USA. ¹¹These authors contributed equally: Zhongling Wang, Xiangdong Xue. ¹²e-mail: lypli@ucdavis.edu

ARTICLES



Dual-contrast enhanced subtraction imaging (DESI)

Scheme 1 Schematic illustration of the TMRET nanotechnology and DESI. Mn^{2+} conjugated to pheophorbide a serves as both an 'enhancer' in the T_1 MRI signal and a 'quencher' in the T_2 MRI signal, whereas the SPIO nanoparticle acts as an 'enhancer' in the T_2 MRI signal and a 'quencher' in the T_3 MRI signal.

by the integrity of the micelles. Furthermore, a complementary postimaging processing and reconstruction method, 'dual-contrast enhanced subtraction imaging' (DESI), is introduced for a better implementation of the dual T_1 and T_2 MRI signal changes. We evaluated this TMRET nanotechnology platform integrated with DESI for the non-invasively and quantitatively imaging of biological targets within the tumour, for example, glutathione (GSH), the key sensing and imaging molecule for redox-responsive nanoplatforms 11,12 . This strategy can be applied to different micellar nanostructures and engineered to respond to other biological markers, such as acidic tumour pH. The proposed TMRET nanoprobe combined with the DESI technique was applied to detect very small intracranial tumours.

TMRET and mechanisms

P-Mn was synthesized by chelating Mn²⁺ to pheophorbide a. The changes in optical behaviours of pheophorbide a suggested the successful synthesis of P-Mn (Supplementary Fig. 1)¹³⁻¹⁵. Then, P-Mn and SPIO (5 nm) were coloaded into a disulfide crosslinked micelle (DCM) to form the TMRET nanoprobes (DCM@P-Mn-SPIO). DCM@P-Mn-SPIO was ~81 nm in diameter (Fig. 1a) and showed a spherical nanostructure that evenly constrained a cluster of SPIOs (Fig. 1b). On the addition of reductive GSH (for disulfide bond cleavage) and sodium dodecyl sulfate (SDS) (for micelle disruption), DCM@P-Mn-SPIO disassembled from 81 to 12 nm (Fig. 1c), and the morphology changed to dispersed small SPIOs (Fig. 1d).

The DCM@P-Mn-SPIO exhibited a payload releasing profile dependent on GSH concentration (Fig. 1e). The payload release can also be triggered by adding GSH at a specific time (Fig. 1f). These results indicate that DCM@P-Mn-SPIO can be responsively dissociated by its molecular target, GSH.

The nanoprobe with a particular ratio of P–Mn to SPIO (1:0.025 by mass) was chosen for the subsequent studies because this ratio showed the most substantial quenching and recovery in T_1 and T_2 signals (Supplementary Fig. 2). Then, the T_1 and T_2 dual-quenching effect of the TMRET nanoprobes was explored. DCM@P-Mn with a single T_1 contrast and DCM@SPIO with a single T_2 contrast were employed as controls (Supplementary Fig. 3). For the TMRET nanoprobe, T_1 -weighted imaging (T_1 WI) and a colour-coded T_1 map both showed obvious T_1 quenching effects (Fig. 1g) when compared with that of DCM@P-Mn (control) at an identical concentration of P-Mn (0.1 mM). A similar MR quenching phenomenon in T_2 -weighted imaging (T_2 WI) and T_2 maps was also observed (Fig. 1h). When the T_1 and T_2 contrast agents were coloaded in DCM@P-Mn-SPIO, T_1 relaxivity (r_1) reduced substantially to 1.23 mM⁻¹ s⁻¹, and T_2 relaxivity (r_2) decreased dramatically to $11.7 \,\mathrm{mM^{-1}\,s^{-1}}$ (Supplementary Table 1). By comparison, DCM@P-Mn showed an r_1 of 5.2 mM⁻¹ s⁻¹ and the r_2 of DCM@SPIO was 88.8 mM⁻¹ s⁻¹ (Supplementary Fig. 4 and Supplementary Table 2). The changes of r_1 and r_2 further confirmed the dual T_1 and T_2 quench of the TMRET nanoprobe. We then investigated the dual T_1 and T_2 signal recovery of the TMRET nanoprobe. When the TMRET nanoprobe

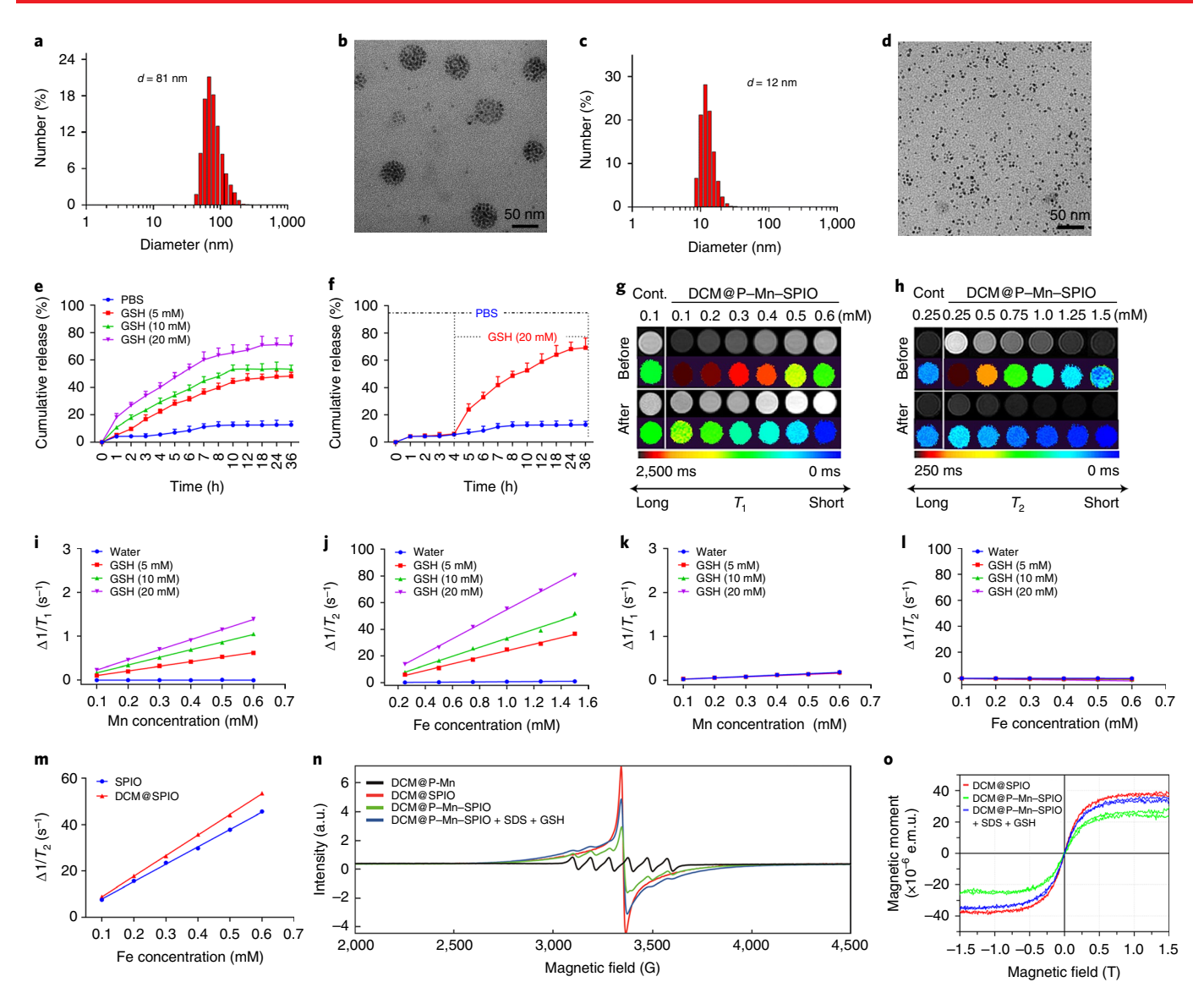


Fig. 1 | TMRET nanoprobes and the T_1/T_2 dual-quenching properties, as well as the mechanism. a,b, Diameter distributions measured by dynamic light scattering (a) and TEM micrograph (b) of DCM@P-Mn-SPIO. c,d, Diameter distributions (c) and TEM micrograph (d) of disassembled DCM@P-Mn-SPIO treated with 20 mM GSH and 3 mg mL⁻¹ SDS for 24 h. To observe changes in morphology, five experiments were repeated independently with similar results. e, The release profiles of pheophorbide a from DCM@P-Mn-SPIO in the presence of different GSH concentrations (0, 5, 10 and 20 mM). Values are reported as mean ± s.d. (n = 3). f, GSH-responsive release profiles (n = 3) of pheophorbide from DCM@P-Mn-SPIO on the delayed addition of GSH (20 mM) at 4 h. Values are reported as mean ± s.d. (n = 3). g,h, T_1 WI and the colour-coded T_1 map (g) and T_2 WI and the colour-coded T_2 map (h) of DCM@P-Mn-SPIO before and after the payload release (triggered by GSH). i,j, The changes in $1/T_1$ values ($\Delta 1/T_1$) (i) and $1/T_2$ values ($\Delta 1/T_2$) (j) of DCM@P-Mn-SPIO at different concentrations before and after incubation with GSH (0, 5, 10 and 20 mM) and SDS. k,l, The changes in $\Delta 1/T_1$ of DCM@P-Mn (k) and $\Delta 1/T_2$ (l) of DCM@SPIO at different concentrations before and after incubation with GSH and SDS. m, T_2 values of free SPIO (75.04 mM⁻¹s⁻¹) and DCM@SPIO (88.97 mM⁻¹s⁻¹). n, EPR spectroscopy studies of DCM@P-Mn, DCM@SPIO and DCM@P-Mn-SPIO in the absence and presence of GSH and SDS. o, Magnetic moment of DCM@SPIO, DCM@P-Mn-SPIO and DCM@P-Mn-SPIO with SDS and GSH, measured over the same sample volume with the background subtracted by a vibrating-sample magnetometer. For the results in g-o, three experiments were repeated independently with similar results. To ensure the concentrations of all the samples were consistent, we added the same volume of water to other samples if a SDS + GSH solution was introduced to one sample. Cont, control; e.m.u., electromagnetic unit.

was dissociated, its T_1 and T_2 signal was recovered as the distance between P–Mn and SPIO increased (Fig. 1i,j). The T_1 and T_2 signal recovery of DCM@P–Mn-SPIO was dependent on GSH concentration. In contrast, DCM@P–Mn and DCM@SPIO did not exhibit 'on' and 'off' switchable MR signals that corresponded to the integrity of the nanoprobes (Fig. 1k,l).

The mechanisms of T_1 and T_2 quenching in the TMRET nanoprobe were investigated. There are extensive reports on the quenching effect of r_1 by a strong magnetization of T_2 contrast materials,

such as SPIO 9,16,17 . The T_2 quenching effect, however, is poorly understood. We found that the $1/T_2$ relaxation time (R_2) of DCM@ SPIO increased slightly compared with that of disperse SPIO nanoparticles (Fig. 1m and Supplementary Fig. 5), which ruled out the possibility that T_2 quenching was induced by SPIO aggregation 18 . We then proposed two possible mechanisms that could underlie the T_2 quenching effect. First, the dipole field experienced by water from the DCM@P-Mn-SPIO can be approximated as the sum of the fields from SPIO and P-Mn. The SPIO possesses

an average magnetic dipole field along the magnetic field direction, whereas P-Mn was measured to be strongly diamagnetic either when encapsulated in the DCM or when released (Supplementary Fig. 6); P-Mn is composed of a diamagnetic pheophorbide a and a paramagnetic Mn^{2+} , and the latter makes it an effective T_1 contrast agent (inset of Supplementary Fig. 6). For a range of magnetic fields and P-Mn to SPIO ratios, the net field components can match the diamagnetic field from the surrounding water. This would make the micelle 'invisible' to the protons and thus quench the T_2 relaxation, although to achieve an exact cancellation in practice is unlikely. Second, attaching molecules to the surface of SPIO has been reported to decrease the net moment of the particle¹⁹. It is known that Mn and Fe have a negative exchange interaction, which results in a non-collinear antiferromagnetic configuration in their binary alloy²⁰. In this case, the Mn²⁺ in P-Mn may interact with SPIO, which reduces the net moment of SPIO. Both mechanisms result in a reduced effective magnetic moment of DCM@P-Mn-SPIO, which suppresses the dipole fields. These weakened dipole fields would extend the transverse relaxation time of the surrounding water protons to produce an increase in the T_2 relaxation time. Once the DCM@P-Mn-SPIO is treated with GSH + SDS, the P-Mn and SPIO become dispersed and both mechanisms cease, and the T_2 contrast would recover (Fig. 1h).

In support of these hypotheses, electron paramagnetic resonance (EPR) and magnetic measurements were performed. In EPR spectra (Fig. 1n), DCM@P-Mn showed a typical EPR spectrum of the Mn ion²¹, whereas DCM@SPIO exhibited the characteristic peaks of SPIO²². Interestingly, the characteristic peaks of both Mn²⁺ and SPIO dramatically decreased, but can recover when the TMRET nanoprobe is broken down (Supplementary Fig. 7). These results indicate that some electrons in DCM@P-Mn-SPIO are no longer free to rotate, potentially being constrained by the magnetic coupling proposed in the second mechanism. The magnetic measurement (Fig. 10) showed a reduction in the magnetization on encapsulation, and a subsequent recovery after GSH+SDS treatment. These results are consistent with the diamagnetic contribution reducing the dipole field from the TMRET nanoprobe (the first mechanism) and the Mn-ion inducing a non-collinear or antiferromagnetic spin texture in the SPIO (the second mechanism). The two mechanisms work synergistically to suppress the dipole fields from the DCM@P-Mn-SPIO and quench r_1 and r_2 (Fig. 2). T_1 contrast agents help relax protons in the surrounding water through a fast spin fluctuation¹¹, whereas r_2 is mainly affected by the dipole– dipole interaction between water protons and the SPIO or TMRET nanoprobe when SPIO and P-Mn are encapsulated. In the off state, the dipole field from the nanoprobe is small, which makes it ineffective in reducing the transverse magnetization of water protons and results in a longer T_2 . Simultaneously, the T_1 contrast agent has a slow spin fluctuation due to the magnetic field from the T_2 contrast agent (SPIO), and is thus also ineffective in relaxing water protons. In the on (activated) state, Mn is decoupled from the SPIO and regains a fast spin fluctuation, which decreases T_1 , and the SPIO recovers its magnetic moment, which helps relax the surrounding water protons. This leads to enhancements in both T_1 and T_2 imaging after dispersion.

Evaluation of the imaging platform in the biological system

This stimuli-responsive TMRET nanoplatform enabled an accurate and quantitative imaging of biological targets. We previously reported that DCM can retain its structural stability and minimize the payload release in blood circulation and allow for an efficient release triggered by GSH at tumour sites^{23–25}. First, the TMRET nanoprobe was proved to have good biocompatibility at the cellular level (Supplementary Fig. 8). Then, we incubated the TMRET nanoprobes with PC-3 tumour cells, PC-3 cells treated with GSH inhibitor (L-buthionine sulfoximine (LBS)^{26,27}) and normal prostate cells

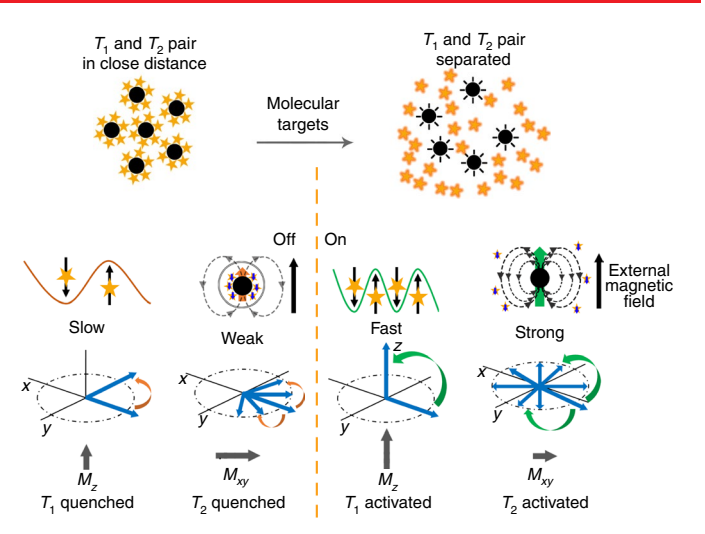
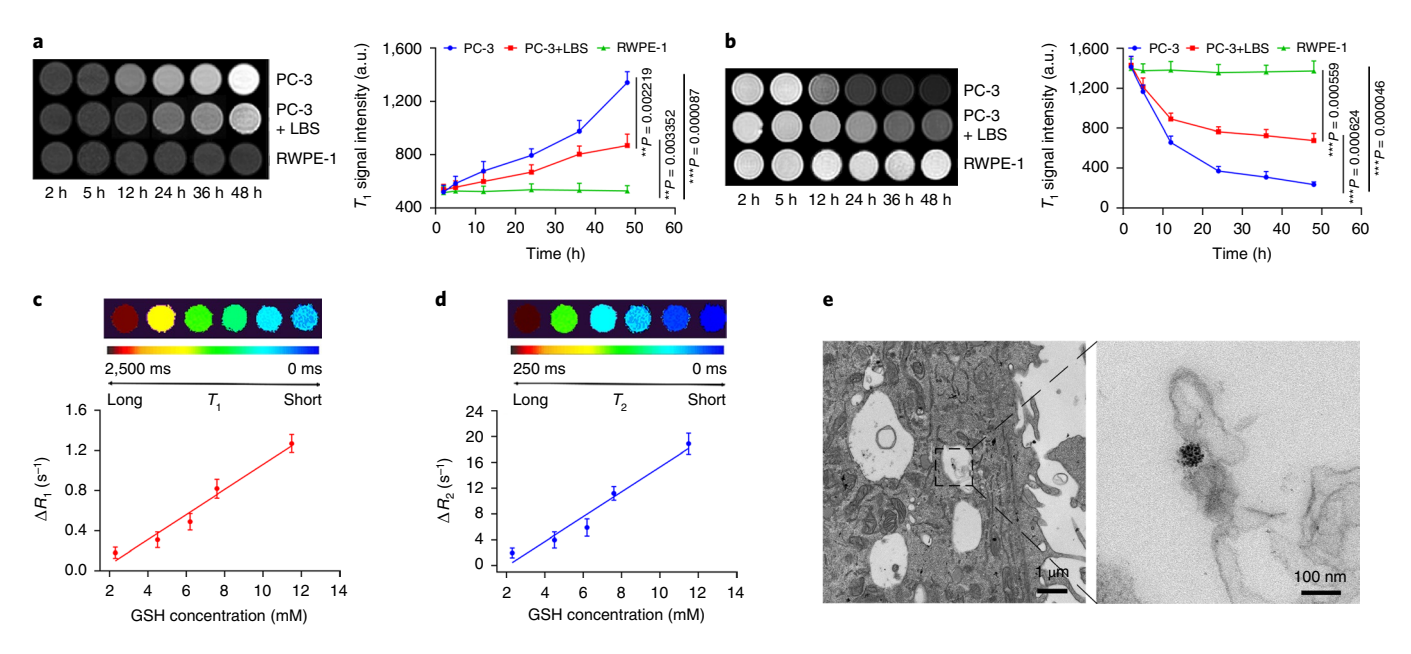


Fig. 2 | Illustration of the mechanism of T_1 **and** T_2 **quenching and recovery in the TMRET nanoprobe.** The black circles denote SPIO and the gold stars denote P-Mn. The gold and green arrows on SPIO indicate magnetization. Different lengths represent the strength of magnetization. Off state: T_1 and T_2 contrast agents are coloaded into DCM with specific concentration ratios. The spin fluctuation of the T_1 contrast agent is slowed, the effective magnetic field from the T_2 contrast agent is weakened and the diamagnetic field further reduces the effective dipole field. This leads to quenched T_1 and T_2 relaxation rates. On state: T_1 and T_2 contrast agents are separated. The fast spin fluctuation of the T_1 contrast agent and the strong magnetic field from the T_2 contrast agent relax the water protons effectively. This leads to enhanced T_1 and T_2 relaxation rates. The black arrow on the gold star represents the paramagnetic contribution from the Mn ion, whereas the blue arrow on the gold star represents the total magnetic contribution from the paramagnetic Mn ion and diamagnetic pheophorbide a.

(RWPE-1), and tested the T_1 and T_2 signal recovery temporally. As shown in Fig. 3a,b, DCM@P-Mn-SPIO exhibited a time-dependent activation of both T_1 and T_2 signals when incubated with PC-3 cells at a high GSH concentration (11.5 mM). Alternatively, DCM@P-Mn-SPIO did not show an obvious T_1 and T_2 signal recovery in RWPE-1 with a lower GSH level (1.89 mM). To verify if DCM@P-Mn-SPIO specifically responded to GSH, LBS was incubated with PC-3 cells to suppress the intracellular GSH level. The DCM@P-Mn-SPIO in the LBS-treated PC-3 cells (GSH was measured as 2.3 mM) showed substantially less MR signal responsiveness than the normal PC-3 cells, which indicates that GSH was the key factor for the activation of the MR signals. In PC-3 cells with different concentrations of GSH (adjusted by LBS), the relaxation rates ΔR_1 ($R_1 = 1/T_1$) and ΔR_2 $(R_2 = 1/T_2)$ increased linearly with the intracellular GSH level (Fig. 3c,d and Supplementary Table 3), which offers the possibility for the TMRET nanoprobe to quantitatively measure the GSH level in biological systems. In PC-3 cells, an obvious SPIO cluster was found inside of the cells by transmission electron microscopy (TEM) (Fig. 3e), which indicates that the TMRET nanoprobe is internalized by tumour cells.

We then quantitively investigated the correlation between the intratumoural GSH level and the MRI signal of the TMRET nanoprobe. The DCM@P-Mn-SPIO was intravenously (i.v.) injected into the tumour-bearing mice (Fig. 4a) for MRI analysis. We found that the ΔR_1 and ΔR_2 increased linearly with the intratumoural GSH concentrations (Fig. 4b,c), which indicates that the TMRET nanoprobes are potentially useful for the in vivo quantitative analysis of molecular target, such as GSH, in a non-invasive manner.

We then evaluated the in vivo performance of TMRET nanoprobes. DCM@P-Mn-SPIO, DCM@P-Mn and DCM@SPIO were i.v. administrated to PC-3 tumour-bearing mice. As shown in Fig. 5a,



 T_1 and T_2 MRI contrast enhancements in the DCM@P-Mn-SPIO group were not distinguishable within 1h but showed an obvious increase at 12h. The contrast remained high for another 12h, and then decreased in 48 h. The T_1 signal-to-noise ratios (SNRs) increased sharply after the administration of DCM@P-Mn-SPIO and gradually grew by 54.9% at 24h postinjection, whereas the T_2 SNR decreased correspondingly by 56.3% (Fig. 5b). In the DCM@P-Mn and DCM@SPIO groups, the MRI contrast enhancement of the tumours increased much faster than that of DCM@P-Mn-SPIO. The T_1 and T_2 MRI signals started to increase at 1h and remained high at 12 h (Supplementary Figs. 9 and 10). T_2^* imaging that solely depended on the SPIO contents could be considered as the baseline of SPIO accumulation, whereas T_2 mapping not only depended on the SPIO accumulation, but was also affected by the activation of the TMRET pair. We then investigated the accumulation and activation of DCM@P-Mn-SPIO and DCM@SPIO by combining the T_2 and T_2^* MR sequences (Fig. 5c). R_2^* values showed no significant difference between the two groups, which indicates a similar SPIO accumulation at the tumour sites (Fig. 5d). The R_2 values (Fig. 5e) were significantly different between the two groups and reflected the initial T₂ quenching of the DCM@P-Mn-SPIO (from 0 to 1 h) in response to GSH. These results indicated that the MRI signal enhancements of the TMRET probe could be activated by the stimuli at the tumour site. The tumours and major organs were collected for haematoxylin and eosin (H&E) staining (Supplementary Fig. 11) and no obvious abnormities were observed.

Dual contrast-enhanced subtraction imaging technology

Furthermore, we developed a new DESI technology as a postimaging processing and reconstruction method to leverage the unique T_1 and T_2 TMRET nanoprobes. DESI was carried out by subtraction of the positive T_1 signal from the negative T_2 signal that switched from off to on to enhance the MR contrast of the targeted sites. We

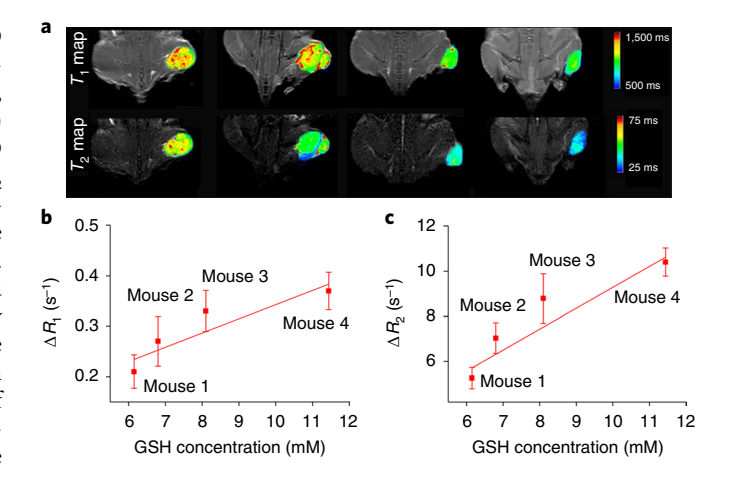


Fig. 4 | The relationship between the MRI relaxation rates and the concentrations of the molecular target of TMRET. **a**, Quantitative MRI visualization of GSH in tumours (n=3) by using DCM@P-Mn-SPIO as a TMRET nanoprobe. The R_1 and R_2 mapped images of PC-3 tumour-bearing mice with different levels of GSH (6.15, 6.80, 8.10 and 11.44 mM) quantitatively determined by using ThiolTracker Violet. **b,c**, Plots of ΔR_1 (**b**) and ΔR_2 (**c**) of the tumours versus GSH concentration in the tumours (n=3). The ΔR_1 values at the tumour sites were measured to be 0.21, 0.27, 0.33 and 0.37 s⁻¹ and the ΔR_2 values were 5.26, 7.03, 9.79 and 10.40 s⁻¹, corresponding to the concentrations of GSH from 6.15 to 11.44 mM. ΔR_1 and ΔR_2 increased linearly with the GSH concentration in the tumours. Pearson's test was used for the correlation analysis. Curves are presented as mean ± s.d.

first investigated the feasibility of DESI in different model systems, such as an aqueous solution, the muscle of normal mice, cancer cell lines and tumour xenografts. In an aqueous solution, T_1 and

ARTICLES

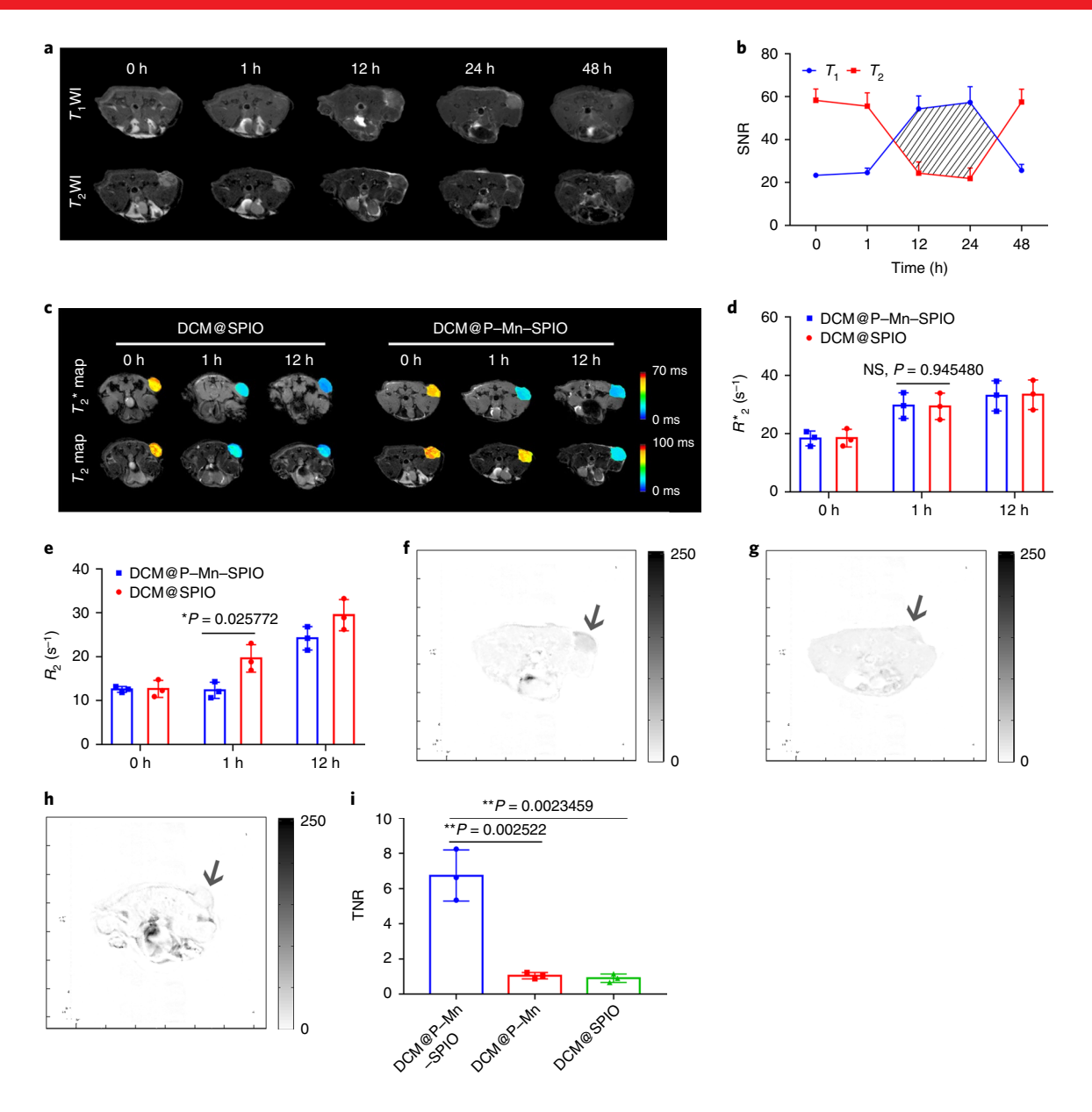


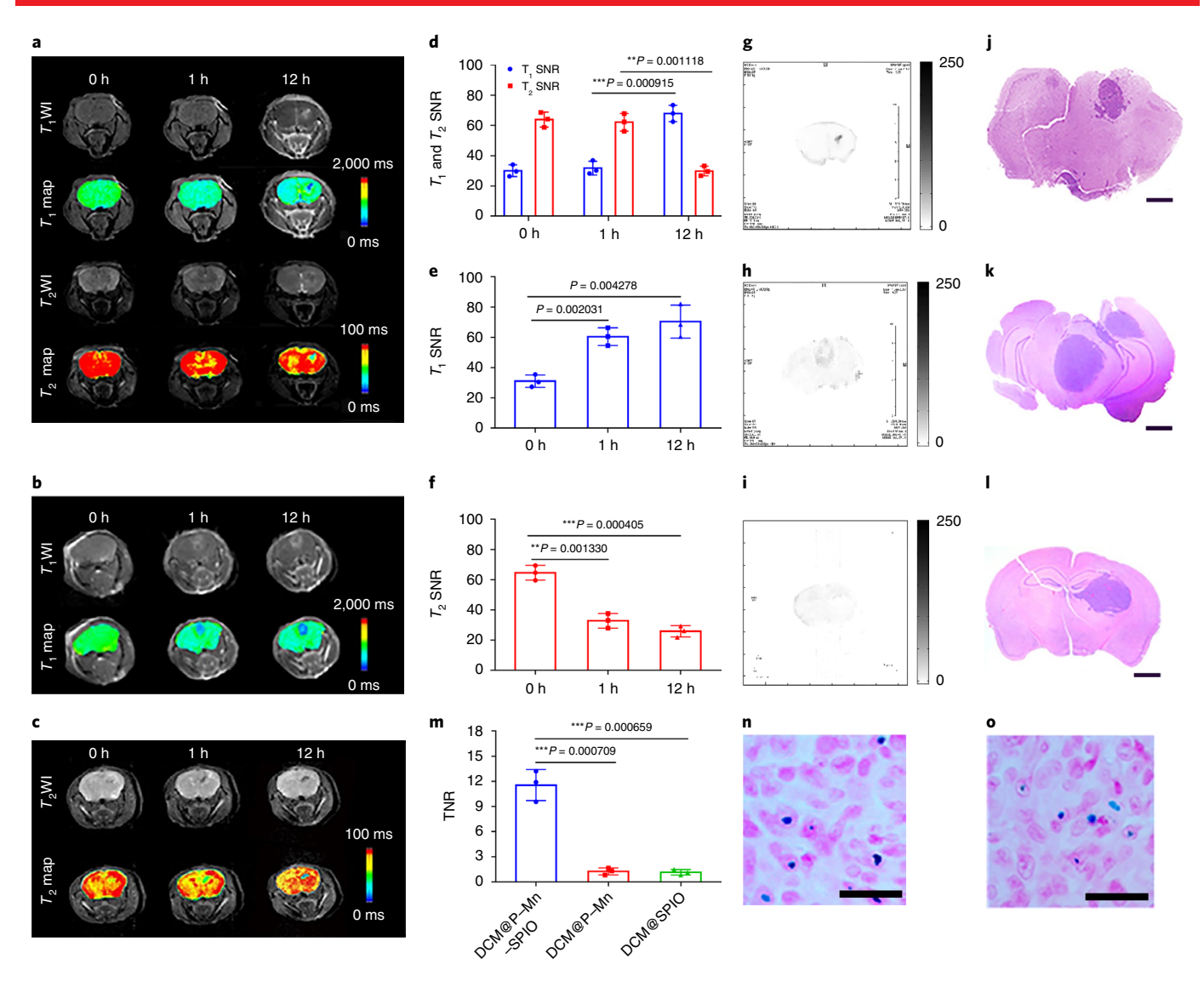
Fig. 5 | In vivo MRI of tumours using DCM@P-Mn-SPIO. a, T_1 WI and T_2 WI of PC-3 tumour-bearing mice (n = 3) after the injection of DCM@P-Mn-SPIO. **b**, SNR and the applicable DESI area of DCM@P-Mn-SPIO in the tumour (n = 3). The shaded area represents the effective T_1 and T_2 DESI area. **c**, The colour-coded T_2 * and T_2 map images of DCM@SPIO and DCM@P-Mn-SPIO. Three experiments were repeated independently with similar results. **d**, **e**, R_2 * (**d**) and R_2 (**e**) of the tumours (n = 3) treated by DCM@SPIO and DCM@P-Mn-SPIO at different time points. **f-h**, DESI subtraction images of DCM@P-Mn-SPIO (**f**), DCM@P-Mn (**g**) and DCM@SPIO (**h**) groups at 12 h after the probe administration (greyscale). The arrows point to the tumours. Three experiments were repeated independently with similar results. **i**, TNR of DCM@P-Mn-SPIO-treated tumours (n = 3). DCM@P-Mn and DCM@SPIO were employed as control groups. Data presented as mean \pm s.d. The two-tailed Student's t-test was employed for the statistical analysis. NS, not significant; *t, <0.05; *t*t, <0.01.

 T_2 MRI signals of DCM@P–Mn–SPIO were detected at concentrations as low as 0.003 mM; further, the T_1 signal intensity was always higher than the T_2 signal intensity (Supplementary Fig. 12). When injected into the muscle of mice, a concentration of DCM@P–Mn–SPIO above 0.06 mM was compatible with DESI (Supplementary Fig. 13). In PC-3 cells, the T_1 signal intensity of DCM@P–Mn–SPIO was greater than the T_2 intensity (Supplementary Fig. 14a). However, DCM@P–Mn–SPIO did not exhibit a higher T_1 signal in PC-3 cells with LBS (Supplementary Fig. 14b) or in normal prostate cells (Supplementary Fig. 14c), due to their low GSH level. In the mouse tumour model, the optimal time window for DESI was 12–24 h (Fig. 5b). DESI was then applied to enhance the

image contrast of the MRIs in Fig. 5a, with the results in Fig. 5f and Supplementary Fig. 15. DESI was not applicable for processing images obtained with a single contrast agent. The DESI images acquired from mice treated with DCM@P-Mn (Fig. 5g) and DCM@SPIO (Fig. 5h) only exhibited dim tumour outlines. The tumour-to-normal-tissue ratio (TNR) of DCM@P-Mn-SPIO was dramatically higher than those of DCM@P-Mn and DCM@SPIO (Fig. 4i) based on DESI processing.

Diagnosis of small intracranial brain tumours

High TNRs are critical to the successful detection of early-stage cancer by imaging approaches^{28,29}. The TMRET nanoprobe was silent in



blood circulation but visible within the tumour. The complementary DESI technology further suppressed the background signal and enhanced the tumour contrast. This integrated imaging platform with TMRET nanotechnology and DESI is expected to achieve the highest possible TNR so far, and is therefore particularly suitable for early cancer detection. We evaluated the capability of this platform to detect early-stage intracranial tumours in a patient-derived xenograft mouse model of glioma (12FLR). In Fig. 6a, at 12h after i.v. injection of DCM@P-Mn-SPIO, both the T_1 and the T_2 MR contrasts in the intracranial tumour were enhanced substantially. The T_1 and T_2 dynamic enhancements (Fig. 6d) from the control groups elevated much faster than that of the TMRET nanoprobe and reached a plateau within a short time (for example, 1 h). The TMRET

nanoprobe showed a gradual increase in MR signal due to the GSH activation, and both the R_1 and R_2 at tumour sites increased dramatically at 12h postinjection (Supplementary Fig. 16a,b). However, DCM@P–Mn (Fig. 6b) and DCM@SPIO (Fig. 6c) enhanced the tumour MR signal at 1 and 12h postinjection (Supplementary Fig. 16c,). The SNRs at tumour sites of mice treated with DCM@P-Mn (Fig. 6e) and DCM@SPIO (Fig. 6f) started to increase at 1h, which indicates the single MRI signal was always on. Then, we utilized the DESI technique to enhance the TNR of DCM@P-Mn-SPIO group. The subtraction imaging results showed that the signal of normal brain tissue could be dramatically reduced, which further highlighted the tumour area (Fig. 6g and Supplementary Fig. 17). In the DCM@P–Mn and DCM@SPIO groups, the DESI technique

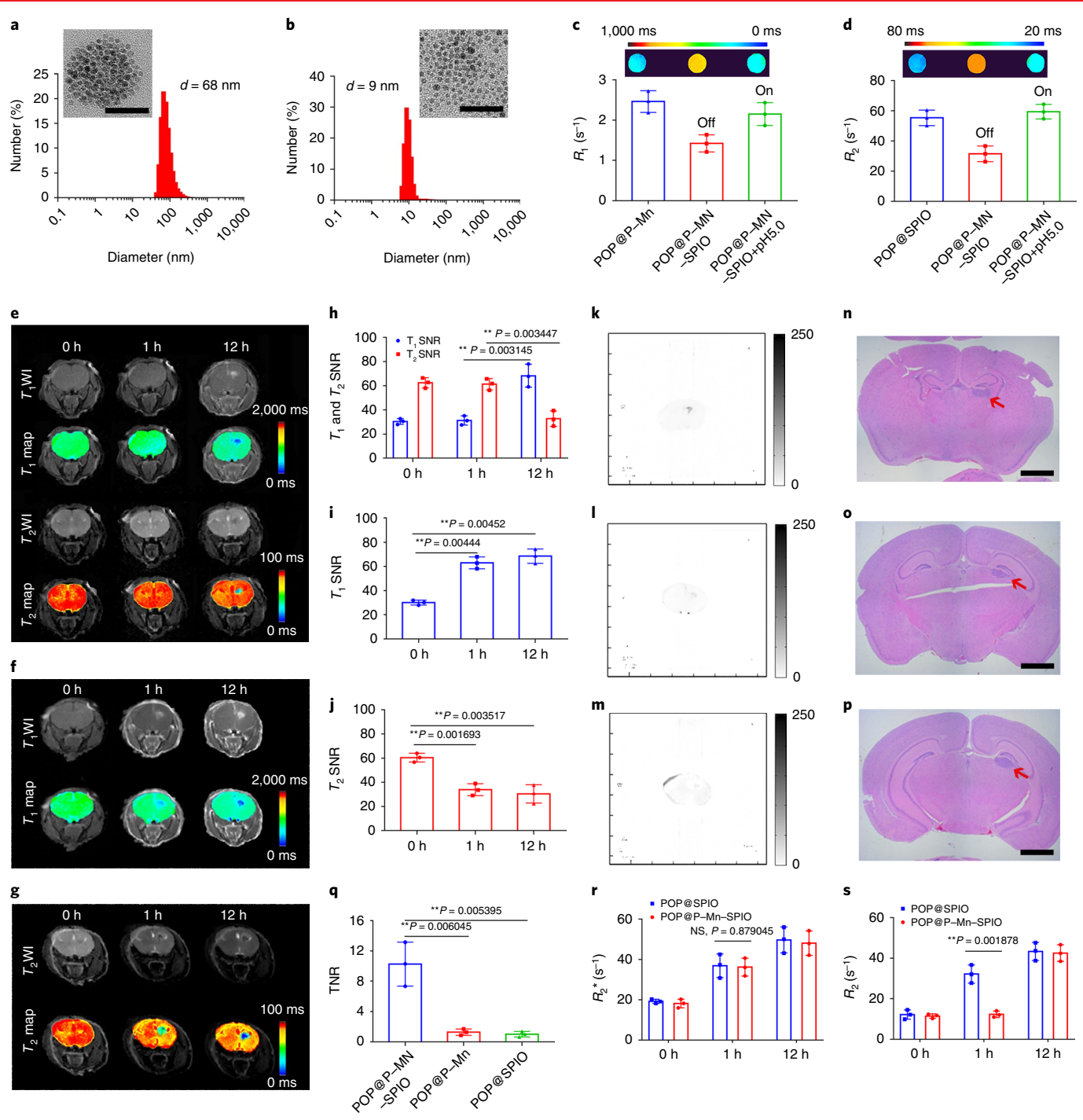


Fig. 7 | Application of TMRET nanotechnology and DESI on a pH-responsive POP@P-Mn-SPIO. a,b, The diameter distribution and morphology of POP@P-Mn-SPIO (**a**) and POP@P-Mn-SPIO (**b**) treated with acidic pH (5.5). Scale bars, 50 nm. Three experiments were repeated independently with similar results. **c,d**, R_1 (**c**) and R_2 (**d**) quenching behaviours of POP@P-Mn-SPIO (n=3). R_1 and R_2 can be recovered by stimulating with acidic pH (5.5). **e**, T_1 WI and T_2 will and T_2 mapped images of mice (n=3) treated with POP@P-Mn-SPIO. **f**, T_1 WI and T_1 mapped image of mice (n=3) treated with POP@P-Mn-SPIO. **h-j**, T_1 and T_2 SNRs of POP@P-Mn-SPIO- (**h**), T_1 SNR of POP@P-Mn-SPIO- (**i**) and T_2 SNR of POP@SPIO- (**j**) mediated MRI of mice bearing an orthotopic brain tumour (n=3). **k-n**, DESI processing of the T_1 WI and T_2 WI image in **f** (**l**) and of the T_2 WI image in **g** (**m**). Scale bars, greyscale. **n-p**, Histopathology of the whole brains of POP@P-Mn-SPIO-treated (**n**), POP@P-Mn-treated (**o**) and POP@SPIO-treated (**p**) mice. The red arrows denote the orthotopic brain tumours. Scale bar, 1 mm. Three experiments were repeated independently with similar results. **q**, TNRs of POP@P-Mn-SPIO-treated tumours (n=3) based on DESI. POP@P-Mn and POP@SPIO were employed as control groups. **r,s**, R_2^* (**r**) and R_2 (**s**) of the tumours (n=3) treated by POP@SPIO and POP@P-Mn-SPIO at different time points. The two-tailed Student's t-test was employed for the statistical analysis. Data presented as mean \pm s.d. NS, not significant; **P < 0.01.

was not applicable. The subtraction images showed a dim tumour outline in the brain (Fig. 6h,i and Supplementary Fig. 17). With DESI, the TNR of DCM@P-Mn-SPIO reached 11.6, whereas those

of DCM@P-Mn and DCM@SPIO were 1.25 and 1.09, respectively (Fig. 6m), which demonstrated that TMRET equipped with DESI can dramatically enhance the TNR. The H&E-stained whole-brain

sections confirmed the location of the tumours (Fig. 6j-l). In the DCM@P-Mn-SPIO group, the tumour size in the cerebrum was approximately 0.75 mm³ (Fig. 6j). Prussian blue stain (to indicate the ferric iron) confirmed that the iron-containing nanoparticles, which included DCM@P-Mn-SPIO (Fig. 6n) and DCM@SPIO (Fig. 60), accumulated in orthotopic brain tumour tissue.

To broaden the applications of the TMRET technique, we also measured the TMRET probe on a 3.0T and 9.4T MRI scanner, respectively. Supplementary Figs. 18 and 19 show that the T_1 and T_2 of DCM@P-Mn-SPIO can be quenched and readily recovered, which supports that the TMRET system is stable and can be broadly applied to MRI scanners with different magnetic fields. This increases the potential for TMRET nanotechnology to be translated into clinical use. To test if the TMRET technique is applicable to different nanocarriers and molecular targets, we developed two new probes that can realize the T_1 and T_2 dual quench and recovery. First, an amphiphilic polymer (1,2-distearoyl-phosphatidylethanolamine-methyl-polyethylene glycol 2000, DSPE-PEG₂₀₀₀) was employed to encapsulate our TMRET pair. The DSPE-PEG readily constrained the TMRET pair in a spherical nanostructure (Supplementary Fig. 20a) and can be dissociated into smaller nanoparticles (Supplementary Fig. 20b). The R_1 and R_2 of DSPE-PEG@P-Mn-SPIO were quenched when the nanostructure was intact and recovered in the presence of SDS (Supplementary Fig. 20c,d), which indicates that our TMRET pair is applicable to other micellar systems that constrain the hydrophobic contrast agents tightly. We also developed a similar telodendritic nanocarrier (PEG₅₀₀₀-OH₈-PPBA (POP); PPBA, porphyrin phenylboronic acid), which could be responsively dissociated on exposure to acidic pH. The chemical structure and characterization of POP are shown in Supplementary Figs. 21-23 and in Supplementary Figs. 24 and 25, respectively. The TMRET pair was encapsulated into POP to form a new pH-responsive TMRET probe (POP@P-Mn-SPIO). The particle size changes (Fig. 7a,b) indicated that POP@P-Mn-SPIO can be broken down by acidic pH. The R_1 (Fig. 7) and R_2 (Fig. 7d) of POP@P-Mn-SPIO can also be quenched and recovered on acidic pH stimulation. In a patient-derived xenograft mouse model with intracranial glioma, the POP@P-Mn-SPIO detected ultrasmall intracranial tumours with very high TNRs (Fig. 7e-q and Supplementary Fig. 26). The T_2^* acquisition (Fig. 7r,s) supported that the initial T₂ quenching and recovery of the POP@P-Mn-SPIO were caused by the MRI signal activation.

Conclusions

We designed a unique TMRET platform with a tailored DESI technique that makes MRI much more sensitive and selective than the conventional techniques used in cancer diagnosis. This is due to the following advantages: (1) a preferential tumour accumulation endows MRI with a high tumour selectivity, (2) the activation by intrinsic tumour stimuli increases the TNR, (3) a dual-modal, subtraction-based, high-sensitivity MRI for the diagnosis of early-stage small lesions and (4) the ultrahigh TNR may highlight the tumour margin to improve the accuracy of MRI-guided surgical procedures. We believe that our new imaging platform has great clinical potential for the diagnosis of cancers and other diseases.

Online content

Any methods, additional references, Nature Research reporting summaries, source data, extended data, supplementary information, acknowledgements, peer review information; details of author contributions and competing interests; and statements of data and code availability are available at https://doi.org/10.1038/s41565-020-0678-5.

Received: 14 February 2018; Accepted: 18 March 2020;

Published online: 25 May 2020

References

- Liu, G. L. et al. A nanoplasmonic molecular ruler for measuring nuclease activity and DNA footprinting. Nat. Nanotechnol. 1, 47-52 (2006).
- Nguyen, A. W. & Daugherty, P. S. Evolutionary optimization of fluorescent proteins for intracellular FRET. Nat. Biotechnol. 23, 355-360 (2005).
- Sönnichsen, C., Reinhard, B. M., Liphardt, J. & Alivisatos, A. P. A molecular ruler based on plasmon coupling of single gold and silver nanoparticles. Nat. Biotechnol. 23, 741-745 (2005).
- 4. Ma, Y. et al. A FRET sensor enables quantitative measurements of membrane charges in live cells. Nat. Biotechnol. 35, 363-370 (2017).
- Schuler, B., Lipman, E. A. & Eaton, W. A. Probing the free-energy surface for protein folding with single-molecule fluorescence spectroscopy. Nature 419, 743-747 (2002).
- Rizzo, M. A., Springer, G. H., Granada, B. & Piston, D. W. An improved cyan fluorescent protein variant useful for FRET. Nat. Biotechnol. 22, 445-449 (2004).
- 7. Biskup, C., Zimmer, T. & Benndorf, K. FRET between cardiac Na+ channel subunits measured with a confocal microscope and a streak camera. Nat. Biotechnol. 22, 220-224 (2004).
- Jares-Erijman, E. A. & Jovin, T. M. FRET imaging. Nat. Biotechnol. 21, 1387-1395 (2003).
- Choi, J. S. et al. Distance-dependent magnetic resonance tuning as a versatile MRI sensing platform for biological targets. Nat. Mater. 16, 537-542 (2017).
- 10. Mizukami, S. et al. Paramagnetic relaxation-based 19F MRI probe to detect protease activity. J. Am. Chem. Soc. 130, 794-795 (2008).
- 11. Mura, S., Nicolas, J. & Couvreur, P. Stimuli-responsive nanocarriers for drug delivery. Nat. Mater. 12, 991-1003 (2013).
- 12. Hong, R. et al. Glutathione-mediated delivery and release using monolayer protected nanoparticle carriers. J. Am. Chem. Soc. 128, 1078-1079 (2006).
- 13. Tam, N. C. M. et al. Porphyrin-lipid stabilized gold nanoparticles for surface enhanced Raman scattering based imaging. Bioconj. Chem. 23, 1726-1730 (2012).
- 14. Lovell, J. F. et al. Porphysome nanovesicles generated by porphyrin bilayers for use as multimodal biophotonic contrast agents. Nat. Mater. 10, 324-332 (2011).
- 15. Xue, X. et al. Trojan horse nanotheranostics with dual transformability and multifunctionality for highly effective cancer treatment. Nat. Commun. 9,
- 16. Zhou, Z. et al. T₁-T₂ dual-modal magnetic resonance imaging: from molecular basis to contrast agents. ACS Nano 11, 5227-5232 (2017).
- 17. Santra, S. et al. Gadolinium-encapsulating iron oxide nanoprobe as activatable NMR/MRI contrast agent. ACS Nano 6, 7281-7294 (2012).
- 18. Mørup, S., Hansen, M. F. & Frandsen, C. Magnetic interactions between nanoparticles. Beilstein J. Nanotechnol. 1, 182-190 (2010).
- Köseoğlu, Y., Yıldız, F., Kim, D. K., Muhammed, M. & Aktaş, B. EPR studies on Na-oleate coated Fe₃O₄ nanoparticles. Phys. Status Solidi C 1, 3511-3515 (2004).
- 20. Kuch, W. et al. Three-dimensional noncollinear antiferromagnetic order in single-crystalline FeMn ultrathin films. Phys. Rev. Lett. 92, 017201 (2004).
- 21. Webb, M. R., Ash, D. E., Leyh, T. S., Trentham, D. R. & Reed, G. H. Electron paramagnetic resonance studies of Mn(II) complexes with myosin subfragment 1 and oxygen 17-labeled ligands. J. Biol. Chem. 257, 3068-3072 (1982).
- 22. Bulte, J. W., Brooks, R. A., Moskowitz, B. M., Bryant, L. H. Jr. & Frank, J. A. Relaxometry and magnetometry of the MR contrast agent MION-46L. Magn. Reson. Med. 42, 379-384 (1999).
- 23. Li, Y. et al. Probing of the assembly structure and dynamics within nanoparticles during interaction with blood proteins. ACS Nano 6, 9485-9495 (2012).
- 24. Li, Y. et al. Well-defined, reversible disulfide cross-linked micelles for on-demand paclitaxel delivery. Biomaterials 32, 6633-6645 (2011).
- 25. Li, Y., Xiao, K., Zhu, W., Deng, W. & Lam, K. S. Stimuli-responsive cross-linked micelles for on-demand drug delivery against cancers. Adv. Drug Deliv. Rev. 66, 58-73 (2014).
- 26. Maeda, H. et al. Effective treatment of advanced solid tumors by the combination of arsenic trioxide and 1-buthionine-sulfoximine. Cell Death Differ. 11, 737-746 (2004).
- 27. Pileblad, E., Magnusson, T. & Fornstedt, B. Reduction of brain glutathione by L-buthionine sulfoximine potentiates the dopaminedepleting action of 6-hydroxydopamine in rat striatum. J. Neurochem. 52, 978-980 (1989).
- 28. Zheng, X. et al. Successively activatable ultrasensitive probe for imaging tumour acidity and hypoxia. Nat. Biomed. Eng. 1, 0057 (2017).
- 29. Hori, S. S., Tummers, W. S. & Gambhir, S. S. Cancer diagnostics: on-target probes for early detection. Nat. Biomed. Eng. 1, 0062 (2017).

Publisher's note Springer Nature remains neutral with regard to jurisdictional claims in published maps and institutional affiliations.

© The Author(s), under exclusive licence to Springer Nature Limited 2020

Methods

Materials. Unless otherwise described, the solvents and chemicals were purchased from commercial sources and used without purification. The pheophorbide a (catalogue no. sc-264070B) was purchased from Santa Cruz Biotechnology, Inc. The SPIO (catalogue no. 700320–5mL) and manganese (II) chloride (catalogue no. 244589–10G) were purchased from MilliporeSigma. The DSPE-PEG $_{2000}$ was purchased from Laysan Bio Inc.

Synthesis of thiolated telodendrimers. The synthesis of thiolated telodendrimers to make DCMs was well-established in our laboratory, and detailed synthesis procedures can be found in previous publications^{24,30-32}.

Synthesis of the POP telodendrimer. Synthesis of PEG-OH₈. Synthesis of acetonide-protected 2,2-bis(hydroxymethyl)propionic acid. For the synthesis, 2 g of 2,2-bis(hydroxymethyl)propionic acid (bis-MPA) (15 mmol), 280 µl of acetone dimethyl acetal (22.4 mmol) and 142 mg of p-toluenesulfonic acid (0.746 mmol) were dissolved in 10 ml of acetone in a 25 ml flask and the mixture was stirred for 6 h at room temperature. Then, 120 µl of triethylamine (0.88 mmol) was added to neutralize the residual acid. A white crystalline product was obtained after the solvent was moved by rotavap.

Synthesis of chlorination of acetonide-2,2-bis(methoxy) propanoic anhydride. The acetonide-2,2-bis(methoxy) propanoic anhydride, obtained as described above, was chlorinated by refluxing in thionyl chloride. Chlorination of acetonide-2,2-bis(methoxy) propanoic anhydride was obtained as a colourless viscous liquid and immediately used in the subsequent reaction.

Synthesis of PEG-K. For the synthesis, 500 mg of CH $_3$ O-PEG $_{5000}$ -NH $_2$, 68 mg of 6-chloro-1-hydroxybenzotriazole, 236 mg of Fmoc-Lys-OH (Fmoc, 9-fluorenyl-methoxycarbonyl) and 62 μ l of diisopropylcarbodiimide were dissolved in 5 ml of dimethylformamide (DMF) in a 10 ml flask and the mixture was stirred for 24 h at room temperature. Then, the mixture was precipitated in diethyl ether and the precipitate was dried under vacuum at room temperature for 24 h to obtain PEG-K-(Fmoc) $_2$. Finally, 5 ml of piperidine (20% in DMF) was used to deprotect the Fmoc to obtain PEG-K by washing with ether three times.

Synthesis of PEG-K-bis-MPA. PEG-K-(Fmoc) $_2$ (200 mg, 0.039 mmol) was dissolved in 2 ml of dry DMF and stirred for 20 min. Acetonide-2,2-bis(methoxy) propanoic anhydride (Ac-MAP; 54.34 mg, 0.312 mmol), diisopropylcarbodiimide (48 µl) and 6-chloro-1-hydroxybenzotriazole (52.8 mg, 0.312 mmol) were added. The mixture was stirred at room temperature for 24h. The flask was opened, and the product filtered off and precipitated in diethyl ether. The precipitate was dried under vacuum at room temperature for 24h to obtain PEG-K-bis-MPA. Finally, the PEG-K-bis-MPA was dissolved in a Dowex H+/methanol mixture to obtain the PEG-OH $_*$.

Synthesis of PEG-OH₈. PEG-OH₄ (1 g), Cl-2,2-bis(methoxy) propanoic acid (290 mg) and 4-dimethylaminopyridine (0.2 equiv. mass) were dissolved in 15 mL dichloromethane (DCM). The mixture was stirred in an ice bath for 1 h and reacted at room temperature for 24 h under $\rm N_2$ atmosphere protection. The product was filtered and precipitated in cold ether. The precipitate was dried under vacuum at room temperature for 24h. Then, the reaction system was dissolved in the Dowex H+/methanol mixture to get PEG-OH₈.

Synthesis of PPBA. Pheophorbide a (237 mg, 0.4 mmol), EDC (306.6 mg, 1.6 mmol) and NHS (184.0 mg, 1.6 mmol) were dissolved in 4 mL of anhydrous DMF and stirred for 20 min. Then the 3-aminophenylboronic acid monohydrate (248.0 mg, 1.6 mmol) was added into the solution. The mixture was stirred at room temperature for 24 h. The product was then filtered and extracted by water/DCM (2:1) for three times. The organic phase was added with 500 mg anhydrous sodium sulfate to remove the residual moisture and evaporated to obtain PPBA by rotavap.

Preparation of POP. PEG-OH $_8$ (10 mg) and PPBA (1 mg) were dissolved in a mixed solution of 2 ml of MeOH and 2 ml and stirred at room temperature for 30 min. The POP monomer is formed by coupling of PEG-OH $_8$ and PPBA through boronate ester bonds.

Synthesis of P–Mn. Based on the method described in a previous publication $^{15},$ pheophorbide a (59.3 mg, 100 $\mu mol)$ and MnCl $_2$ (63 mg, 500 $\mu mol)$ were dissolved in a mixed solution of methanol (8 ml) and pyridine (0.8 ml). The reaction system was refluxed at 60 °C for 2 h. Free Mn²+ was removed by extraction (DCM against water). The P–Mn was dissolved in DCM, and the free Mn²+ was washed off by water. The P–Mn was then aliquoted and dried on a rotavapor.

Preparation of DCM@P-Mn-SPIO. P–Mn, SPIO and thiolated telodendrimers (20 mg) were dissolved in tetrahydrofuran (200 μ l) and dripped into 11 of deionized water with vigorous stirring overnight at 37 °C. The ratios of P–Mn to SPIO were tuned to 1:0.006, 1:0.013, 1:0.025 and 1:0.05. After that, 4 μ l of H₂O₂ was added to oxidize the thiol groups to form intramicellar disulfide crosslinkages based

on our published method. DCM@P-Mn with single T1 contrast and DCM@ SPIO with single T_2 contrast were prepared by using similar procedures with identical amounts of P-Mn or SPIO, respectively. For the following in vitro and in vivo studies, the ratio of P-Mn to SPIO in DCM@P-Mn-SPIO was fixed to 1:0.025. The encapsulation efficiency of P-Mn was 98.3% by measuring the ultraviolence absorbance of the free P-Mn. For the encapsulation of SPIO, it was technically difficult to isolate unloaded SPIO from DCM@P-Mn-SPIO, because both are nanoparticles. The SPIO that we employed is very hydrophobic (the stock was kept in toluene). When we encapsulated SPIO into DCM, we did not find any precipitations, either by the naked eye or by dynamic light scattering measurements. Based on this evidence, we believe the encapsulation efficiency of SPIO is also very high and the actual ratio is close to its reaction ratio. Based on Supplementary Fig. 2, the T_1 and T_2 quench can be realized in different ratios between SPIO and P-Mn, which supports that our probe has good reproducibility and can be made with only a little fluctuation of the ratios between SPIO and P-Mn. Therefore, we recommend making a DESI probe based on our reaction ratio of 1:0.025 without further purification.

Preparation of DSPE-PEG@P-Mn-SPIO and POP@P-Mn-SPIO. The preparation of these two nanoprobes followed the same procedures as used for DCM@P-Mn-SPIO. Briefly, 20 mg of DSPE-PEG or POP, P-Mn and SPIO were dissolved in tetrahydrofuran (200 µl) and dripped into 1 ml of deionized water with vigorous stirring overnight at 37 °C. The ratio between P-Mn and SPIO was set as 1-0.025

Characterization of the TMRET probes and the control probes with single contrast agents. The t-TMRET probes included DCM@P-Mn-SPIO, DSPE-PEG@P-Mn-SPIO and POP@P-Mn-SPIO; the probes with single contrast agents included DCM@P-Mn, DCM@SPIO, DSPE-PEG@P-Mn, DSPE-PEG@ SPIO, POP@P-Mn and POP@SPIO. The size distributions of the nanoprobes (1.0 mg ml⁻¹) were measured by a dynamic light scattering instrument (Nano ZS, Malvern). The morphology was observed by TEM (Talos, L120c, FEI). The samples were made by directly dripping the aqueous nanoparticle solution (1.0 mg ml⁻¹) onto copper grids, and placed at room temperature to dry naturally. The ultraviolet-visible (UV-vis) absorbance was measured by a UV-vis photospectrometer (UV-1800, Shimadzu), and the fluorescence spectra were obtained by a fluorescence photospectrometer (RF6000, Shimadzu). For the optical measurements, which included UV-vis and fluorescence spectra, the cuvette width was 1 cm.

GSH-concentration-related MR relaxivity changes of DCM@P-Mn-SPIO, **DCM@P-Mn and DCM@SPIO.** The R_1 and R_2 values of the DCM@P-Mn-SPIO were measured on a 7.0 T MRI scanner (Bruker Biospec) at 37 °C. Different concentrations of DCM@P-Mn-SPIO were treated with 100 µl of GSH (0, 5, 10 and 20 mM) before MRI. In DCM@P-Mn-SPIO, the concentrations of Mn2+ varied from 0.1 to 0.6 mM, and of SPIO from 2.5 to 15 mM. The R_1 and R_2 values of the DCM@P-Mn-SPIO were measured from 0 to 24h after incubation with GSH in the presence of SDS. The acquisition parameters were set as: T_1WI_1 repetition time (TR) = 200 ms, echo time (TE) = 15 ms, slice thickness = 1 mm, slice spacing = 1 mm, a 100-mm square field of view (FOV) was used with an image matrix of 256 \times 256; T_1 map images, TR = 100-2,000 ms, TE = 14 ms, slice thickness=1 mm, slice spacing = $\overline{1}$ mm, FOV = 10×10 cm, matrix = 256×256 ; T_2 WI, TR = 1,000 ms, TE = 100 ms, slice thickness = 1 mm, slice spacing = 1 mm, a 100-cm² FOV was used with an image matrix of 256 \times 256; T_2 map images, TR = 1,000 ms, TE = 15-225 ms, slice thickness = 1 mm, slice spacing = 1 mm, FOV = 10×10 cm, matrix = 256×256 . Quantitative T_1 and T_2 relaxation maps were reconstructed from datasets using Paravision 4 software. The same method was applied for the relaxivity calculation of DCM@P-Mn (0.1 to 0.6 mM, Mn2+) and DCM@SPIO (0.1 to 0.6 mM, SPIO).

EPR spectroscopy. The samples (DCM@SPIO, DCM@P-Mn, DCM@P-Mn-SPIO) for EPR characterization were prepared using the same procedures as described above, with concentrations of 1.5 mg ml⁻¹ for P-Mn and 0.0375 mg ml⁻¹ for SPIO. The X-band (9.43 GHz) continuous-wave EPR spectra were recorded on a Bruker Biospin EleXsys E500 spectrometer equipped with a super-high Q resonator (ER4122SHQE). All continuous-wave EPR data were acquired under non-saturating conditions at room temperature, with an excitation microwave frequency of 9.87 GHz, microwave power of 0.6325 mW and modulation frequency of 100 kHz.

Magnetometry. DCM@SPIO, DCM@P-Mn-SPIO, DCM@P-Mn-SPIO+SDS+GSH were prepared with 0.5 mg ml of P-Mn and 0.0125 mg ml of SPIO. In addition, we made reference samples without SPIO (DCM, DCM@P-Mn, DCM@P-Mn+SDS+GSH), whose concentrations were kept the same as for the samples that contained SPIO. The same volume of each type of sample was loaded into the same liquid sample holder with a cap from Lake Shore Cryotronics and filled to capacity before the measurement. The sample holder was sonicated by water and acetone and dried before changing samples. Thus, each sample had nominally the same amount of SPIO, due to the identical sample volume and

concentration. Hysteresis loops were measured at room temperature using a vibrating sample magnetometer from the Princeton Measurements Corporation as well as a superconducting quantum interference device (SQUID) magnetometer (MPMS3) from Quantum Design. After the measurements, we subtracted the background using the reference samples. For example, the SPIO signal shown in Fig. 10 was obtained by subtracting the measured signal of the DCM reference sample from DCM@SPIO, removing the background, including sample holder, water and the DCM, from the measured signal. Similarly, DCM@P-Mn-SPIO, DCM@P-Mn-SPIO+SDS+GSH measurements were calibrated against DCM@P-Mn and DCM@P-Mn+SDS+GSH reference samples, respectively. Data from different samples are plotted together in the measured magnetic moment in Fig. 10. Additionally, DCM@P-Mn was calibrated against a DCM reference sample.

Accumulated payload release of DCM@P–Mn–SPIO. The DCM@P–Mn–SPIO solution was prepared to determine the payload release profile. The UV–vis absorbance of P–Mn was measured to determine the payload release. DCM@P–Mn–SPIO (1 mg ml⁻¹ (0.5 ml) PBS solutions with various GSH concentrations (0, 5, 10 and 20 mM) were injected into dialysed cartridges (Pierce Chemical Inc.) with a 3.5 kDa molecular weight cutoff. The cartridges were dialysed against 21 of PBS at 37 °C. In the stimulus-responsive release experiment, GSH (20 mM) was added to the release medium at a specific time (4h). The P–Mn concentrations that remained in the dialysis cartridge at various time points were calculated by the standard curve. The payload release was performed in triplicate to calculate the mean values.

Cell viability assay. To evaluate the biocompatibility of DCM@P-Mn-SPIO, DCM@P-Mn and DCM@SPIO, PC-3 prostate cancer cells were incubated with these nanoprobes and the cell viability was measured by methyl thiazolyl tetrazolium. PC-3 cells were seeded in a 96-well plate with a density of 3×10^5 cells per well, and incubated for 24 h (37 °C, 5% CO₂) until all the cells were completely attached. Then, different concentrations of DCM@P-Mn-SPIO, DCM@P-Mn and DCM@SPIO were added (all the probe concentrations were calculated based on DCM concentrations, which corresponded to 0, 0.1, 0.5, 1 and 5 mg ml $^{-1}$). After incubation for 24h, the media was aspirated and 150 µl of dimethyl sulfoxide was added to dissolve the methyl thiazolyl tetrazolium crystal. Absorbance at 490 nm was measured by using a microplate reader (SpectraMax M3) to assess the cell viability.

In vitro MRI on PC-3 and RWPE-1 cells. In vitro MRI was performed on PC-3 cells with and without GSH inhibitor (LBS² $^{0.27}$), as well as on normal prostate cells (RWPE-1) (1×10 6). The cells were incubated with DCM@P-Mn-SPIO (P-Mn concentration was 40 µg ml $^{-1}$) for 2h, the cells were washed three times with PBS, collected at various time points (2, 5, 12, 24, 36 and 48 h) and fixed in agarose (1 ml, 1.0%) in Eppendorf tubes. MRI was performed on a 7.0 T MR system. T_1 WI were obtained using the following parameters: TR/TE = 250 ms/14 ms, T_2 WI = 1,000 ms/100 ms, slice thickness=1 mm, slice spacing=1 mm, matrix = 256×256 and FOV = 10 cm×10 cm. The T_1 and T_2 signal intensities were measured within the region of interest.

In vitro MRI was further performed on PC-3 cells that were incubated with different concentrations of GSH inhibitor from 0 to 50 μ M for 24 h. After incubation with P–Mn (40 μ g ml⁻¹) for 2 h, the cells were washed three times with PBS and digested with 0.25% trypsin at different time points (2, 5, 12, 24, 36 and 48 h), centrifuged for 3 min and resuspended in agarose (1 ml, 1.0%) in Eppendorf tubes. MRI was performed on a 7.0 T MR system. T_1 map images: TR = 100–2,000 ms, TE = 14 ms, slice thickness = 1 mm, slice spacing = 1 mm, FOV = 10 × 10 cm, matrix = 256 × 256. T_2 map images: TR = 1,000 ms, TE = 15–225 ms, slice thickness = 1 mm, slice spacing = 1 mm, FOV = 10 cm, matrix = 256 × 256.

Cell uptake of DCM@P-Mn-SPIO evaluated by TEM. The cellular uptake of DCM@P-Mn-SPIO was further evaluated by TEM (Talos, L120c, FEI) with an accelerating voltage of 80 kV. In brief, the cells were seeded at a density of 1×10^5 cells per well into an 8-well Permanox slide for 24 h, reaching a confluency of 80%. Then the cells were treated with DCM@P-Mn-SPIO for 2 h at 37 °C. The embedded cells were sectioned (75 nm) and mounted onto 200-mesh copper grids after washing with phosphate buffer.

Tumour xenograft and orthotopic tumour animal models. Nude mice, 4–5 weeks of age, were obtained from Harlan. All the animals were kept under pathogen-free conditions according to AAALAC guidelines, and were allowed to acclimate for at least 4 days prior to any experiments. All animal the experiments were performed under the requirements of institutional guidelines and according to protocol no. 07–13119 approved by the Use and Care of Animals Committee at the University of California, Davis. PC-3 cells in a 200 μ l mixture of PBS suspension and Matrigel (1:1 v/v) were subcutaneously injected into the right flank of nude mice. The tumour sizes for all the nude mice were monitored and recorded weekly. Tumours that reached the longest dimension of 0.8–1.0 cm were used for in vivo MRI. The tumour volume was calculated by the formula (length \times (width)²)/2. For orthotopic or intracranial implantation, 2.5×10^5 12FLR

glioma cells, derived from patient samples and resuspended in $5\,\mu l$ of PBS were injected into the right striatum area of the nude mouse with the aid of a mouse stereotactic instrument (Stoelting). The tumour sizes for all the nude mice were monitored and recorded weekly by the bioluminescence signal of luciferase.

In vivo MRI. PC-3 tumours and orthotopic 12FLR glioma-bearing nude mice (n=3) were scanned on a 7.0 T MRI scanner (Bruker Biospec), with a high-resolution animal coil. The mice were i.v. administrated with $100\,\mu$ l of the nanoprobes and then subjected to MRI at different time points: DCM@P-Mn-SPIO (0,1,12,24 and $48\,h)$, DCM@P-Mn (0,1 and $12\,h)$ and DCM@SPIO (0,1 and $12\,h)$. The concentrations of P-Mn and SPIO were kept at 15 and $0.25\,\mathrm{mg}\,\mathrm{ml}^{-1}$, respectively. All the mice were imaged under the $T_1\mathrm{WI}$ (TR/TE = $300/14\,\mathrm{ms}$) and $T_2\mathrm{WI}$ spin-echo sequences (TR/TE = $1,000/100\,\mathrm{ms}$), the T_1 map image (TR/TE = $100-2,000/14\,\mathrm{ms}$) and the T_2 map image (TR/TE = $1,000/15-225\,\mathrm{ms}$) (slice thickness = $1\,\mathrm{mm}$, slice spacing = $1\,\mathrm{mm}$, FOV = $10\,\mathrm{x}\,10\,\mathrm{cm}$, matrix = $256\,\mathrm{x}\,256$). The mean $T_1\mathrm{WI}$ and $T_2\mathrm{WI}$ signal intensities (S_{mean}) were measured for each tumour. Quantitative T_1 and T_2 maps were reconstructed from datasets using Paravision 4 software. T_1 and T_2 relaxation times were calculated with the Paravision 4 software. Then, the relative SNR (= S_{mean} /(standard deviation of the background signal)) was calculated based on a previously reported method 33 .

 T_2 star measurement. For T_2^* images, the MRI parameters were TR = 1,500 ms, TE = 4.0–61.5 ms, FOV = 8×8 cm and matrix = 256×256. Quantitative T_2^* maps were reconstructed from datasets using Paravision 4 software. R_1 , R_2 and R_2^* were defined as the $1/T_1$, $1/T_2$ and $1/T_2^*$ relaxation times, respectively.

DESI of the MRI. When the MRI study was performed using a $7.0\,\mathrm{T}$ MRI Scanner (Bruker Biospec), MRIs were acquired at the same time point by $T_1\mathrm{WI}$ and $T_2\mathrm{WI}$ sequences with identical MRI geometrical parameters to ensure that the image slices were consistent. The MRIs were co-registered to ensure T_1 -weighted images correspond to the corresponding point of the T_2 -weighted images. Then the images of the skull and surrounding soft tissue of the mouse were removed using ImageJ software.

H&E staining and Prussian blue staining. After humanely killing the mice, we collected the major organs and fixed them in 4% paraformaldehyde. The organs were then sliced and stained by H&E to evaluate the systemic toxicity of our nanoprobes. Prussian blue staining was performed as previously described³⁴ to detect iron-positive cells.

Statistical analysis. All data analyses are shown as mean \pm s.d. The analysis was performed using GraphPad Prism 7.00. The MRI signal intensity, ΔR_1 and ΔR_2 versus GSH concentration, were compared and analysed using univariate analysis of variance and Paravision 4. Pearson's test was used for correlation analysis. Two-tailed Student's t-tests were employed for the statistical analysis. P values <0.05 were considered statistically significant for all the analyses.

Reporting summary. Further information on research design is available in the Nature Research Reporting Summary linked to this article.

Data availability

The data that support the plots within this paper and other findings of this study are available from the corresponding author upon reasonable request.

Code availability

The subtraction imaging was obtained in MATLAB R2013b software by using the following commands:

A = imread ('D: T_1 WI'); B = imread ('D: T_2 WI'); C = imsubtract (A, B); J = imcomplement c;

J, subtraction images of the T_1 - and T_2 -weighted imaging. The last step involved the antiphase processing of subtraction images using MATLAB R2013b software.

References

- Li, Y. et al. A smart and versatile theranostic nanomedicine platform based on nanoporphyrin. Nat. Commun. 5, 4712 (2014).
- Kato, J. et al. Disulfide cross-linked micelles for the targeted delivery of vincristine to B-cell lymphoma. Mol. Pharm. 9, 1727–1735 (2012).
- Xiao, K. et al. Disulfide cross-linked micelles of novel HDAC inhibitor thailandepsin A for the treatment of breast cancer. *Biomaterials* 67, 183–193 (2015).
- Wang, Z. et al. Active targeting theranostic iron oxide nanoparticles for MRI and magnetic resonance-guided focused ultrasound ablation of lung cancer. *Biomaterials* 127, 25–35 (2017).
- Zhang, Z. et al. Facile synthesis of folic acid-modified iron oxide nanoparticles for targeted MR imaging in pulmonary tumor xenografts. *Mol. Imaging Biol.* 18, 569–578 (2016).

Acknowledgements

We thank financial support from the National Institutes of Health (NIH)/National Cancer Institute (R01CA199668), NIH/Eunice Kennedy Shriver National Institute of Child Health and Human Development (R01HD086195), UC Davis Comprehensive Cancer Center Support Grant (CCSG) awarded by the National Cancer Institute (NCI P30CA093373) and National Science Foundation (NSF) (ECCS-1611424 and ECCS-1933527). The acquisition of a magnetic property measurements system (MPMS3) at Georgetown University was supported by the NSF (DMR-1828420).

Author contributions

Y.L., X.X. and Z.W. conceived the idea and designed the TMRET nanoprobe. Z.W. conducted most of the experiments, X.X. assisted with some of the experiments. X.X. and Z.W. analysed the data. X.X. led the revisions of the manuscript. H.L. worked on the POP materials and animal experiments. Y.H. assisted with the animal studies. Z.W. and Z.L. conducted the DESI process. Z.C., L.Q., N.C., D.A.G., X.X. and K.L. performed the magnetic characterization and assisted with the explanation of T_2 quench mechanism. Y.Y. assisted with the MRI data analysis. T.L. assisted

with the design and data analysis of biological experiments. K.S.L., A.Y.L. and K.W.F. provided valuable suggestions on the project methodology. X.X., Y.L. and Z.W. wrote the paper and all the authors commented on the manuscript. Y.L. supervised the project.

Competing interests

Y.L., X.X. and \overline{Z} .W. are the co-inventors on the pending patent application filed by the Regents of the University of California on the TMRET nanotechnology and DESI.

Additional information

Supplementary information is available for this paper at https://doi.org/10.1038/s41565-020-0678-5.

Correspondence and requests for materials should be addressed to Y.L.

Peer review information *Nature Nanotechnology* thanks Jeff Bulte, John Waterton and the other, anonymous, reviewer(s) for their contribution to the peer review of this work.

Reprints and permissions information is available at www.nature.com/reprints.